Progress In Electromagnetics Research, PIER 87, 63–88, 2008

GEOELECTRICAL ANOMALIES IMAGED BY POLAR AND DIPOLAR PROBABILITY TOMOGRAPHY

P. Mauriello

Department of Science and Technology for Environment and Territory
University of Molise
Campobasso, Italy

D. Patella

Department of Physical Sciences
University Federico II
Naples, Italy

Abstract—The 3D probability tomography theory is developed to image polar and dipolar sources of a geophysical field dataset. The purpose of the method is to improve resolution power of buried geophysical targets, using probability as a suitable paradigm allowing all possible equivalent solutions to be included within a single 3D image. The new approach is described by assuming a geophysical field dataset as caused by a discrete number of source poles and dipoles. A few tests are given to show how the combined polar and dipolar tomography can provide a reliable core-and-boundary resolution of the most probable sources of anomalies. An application to the Vesuvius volcano (Naples, Italy) is finally illustrated by analyzing self-potential and geoelectrical datasets collected within the whole volcanic area. A gravity dataset is also analyzed for completeness. The purpose is to get new insights into the Vesuvius shallow structure and hydrothermal system and to outline the features of the deep tectonic depression within which the volcano grew.

1. INTRODUCTION

Probability tomography has been proposed in applied geophysics as a method to virtually explore the subsoil in the search of the most probable emplacement of the sources of the anomalies appearing in a field dataset collected on the ground surface. It has been

formulated for potential field methods, namely self-potential [23, 24], geoelectrical [12, 15, 19, 21], and gravity [13, 14]. In all of these approaches, the buried bodies responsible of the anomalies have been simulated as aggregates of source poles. A pole has been assumed to represent a small cell with uniform electrical charge density in the self-potential method, resistivity in geoelectrics and mass density in gravity. A further extension of the tomography has been made to image aggregates of elementary magnets as responsible of anomalies detected in a magnetic survey [16, 20].

In this paper, we generalize the theory of probability tomography for potential field methods, assuming that a generic dataset can be viewed as the response of a double set of polar and dipolar sources. Dipoles are thus included and assumed to simulate the response due to small cells across a physical discontinuity. Dipole probability tomography is expected to give insight into the spatial extent of a target body by providing an image of the most probable location of its boundaries. The joint analysis of pole and dipole tomographies appears to be a goal of great interest for a better definition of the sources of anomalies.

2. POLAR AND DIPOLAR PROBABILITY TOMOGRAPHY

Let us consider a reference coordinate system with the (x, y)-plane placed at sea level and the z-axis positive downwards, and a 3D datum domain V as drawn in Fig. 1. In particular, the top surface S represents a non-flat ground survey area defined by a height function $z_t(x, y)$, and the bottom surface $z_b(x, y)$ includes the maximum depths at which datum points are attributed. Let $\mathbf{A}(\mathbf{r})$ be a vector anomaly field at a set of datum points $\mathbf{r} \equiv (x, y, z)$, with $\mathbf{r} \in V$. Let us assume that $\mathbf{A}(\mathbf{r})$ can be discretised as [17]

$$\mathbf{A}(\mathbf{r}) = \sum_{m=1}^{M} p_m \mathbf{s}\left(\mathbf{r}, \mathbf{r}_m\right) + \sum_{n=1}^{N} \left(\mathbf{d}_n \cdot \nabla_n\right) \mathbf{s}(\mathbf{r}, \mathbf{r}_n), \tag{1}$$

i.e., as a sum of effects due to M poles, whose m-th element located at $\mathbf{r}_m \equiv (x_m,\, y_m,\, z_m)$ has strength p_m, and N dipoles, whose n-th element located at $\mathbf{r}_n \equiv (x_n,\, y_n,\, z_n)$ is given as strength the operator $\mathbf{d}_n \cdot \nabla_n$, being $\mathbf{d}_n$ its dipole moment. The effect of both the M and N source elements at a datum point $\mathbf{r} \in V$ is analytically described by the same vector kernel $\mathbf{s}(\mathbf{r})$.

We define the information power Λ associated with $\mathbf{A}(\mathbf{r})$ within

V as

$$\Lambda = \int_V \mathbf{A}(\mathbf{r}) \cdot \mathbf{A}(\mathbf{r}) dV, \tag{2}$$

which, using Eq. (1), is expanded as

$$\Lambda = \sum_{m=1}^{M} p_m \int_V \mathbf{A}(\mathbf{r}) \cdot \mathbf{s}(\mathbf{r}, \mathbf{r}_m) dV + \sum_{n=1}^{N} \sum_{\nu=x,y,z} d_{n\nu} \int_V \mathbf{A}(\mathbf{r}) \cdot \frac{\partial \mathbf{s}(\mathbf{r}, \mathbf{r}_n)}{\partial \nu_n} dV. \tag{3}$$

2.1. The Source Pole Occurrence Probability

We consider a generic m-th integral of the first sum in Eq. (3) and apply Schwarz inequality, obtaining

$$\left[\int_V \mathbf{A}(\mathbf{r}) \cdot \mathbf{s}(\mathbf{r}, \mathbf{r}_m) dV \right]^2 \leq \int_V A^2(\mathbf{r}) dV \int_V s^2(\mathbf{r}, \mathbf{r}_m) dV, \tag{4}$$

where $A(\mathbf{r})$ and $s(\mathbf{r}, \mathbf{r}_m)$ are the modulus of $\mathbf{A}(\mathbf{r})$ and $\mathbf{s}(\mathbf{r}, \mathbf{r}_m)$, respectively.

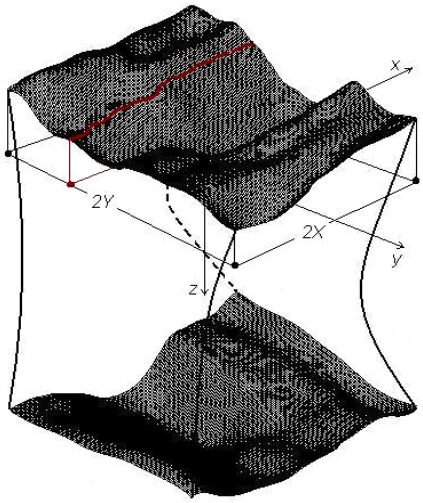

Figure 1. The 3D datum domain, characterized by irregular boundary surfaces. The (x, y)-plane is placed at sea level and the z-axis points into the earth.

From inequality (4) we derive a *source pole occurrence probability* (SPOP) function as

$$\eta_m^{(P)} = C_m \int_V \mathbf{A}(\mathbf{r}) \cdot \mathbf{s}(\mathbf{r}, \mathbf{r}_m) dV, \tag{5}$$

where

$$C_m = \left[\int_V A^2(\mathbf{r}) dV \int_V s^2(\mathbf{r}, \mathbf{r}_m) dV \right]^{-1/2}. \tag{6}$$

The 3D SPOP function satisfies the condition

$$-1 \leq \eta_m^{(P)} \leq +1 \tag{7}$$

and is assumed as a measure of the probability, which a polar source (P-source) of strength p_m at $\mathbf{r}_m$ obtain as responsible of the $\mathbf{A}(\mathbf{r})$ field.

In many geophysical methods, anomaly field and kernel are described by scalar functions, and $\eta_m^{(P)}$ is simply given by

$$\eta_m^{(P)} = C_m \int_V A(\mathbf{r}) s(\mathbf{r}, \mathbf{r}_m) dV, \tag{8}$$

using again Eq. (6) to obtain C_m.

The role of probability for $\eta_m^{(P)}$ is motivated as follows. Generally, a probability measure Ψ is defined as a function assigning to every subset E of a space of states U a real number $\Psi(E)$ such that [4]

$$\Psi(E) \geq 0, \text{ for every } E, \tag{9a}$$

$$\text{if } E \cap F \equiv 0, \text{ with } E, F \subset U, \ \Psi(E \cup F) = \Psi(E) + \Psi(F), \tag{9b}$$

$$\Psi(U) = 1. \tag{9c}$$

Given that the presence of a P-source at a point is independent from the presence of another P-source at another point, the function

$$\Psi_m = \frac{\left|\eta_m^{(P)}\right|}{\int_{V_m} \left|\eta_m^{(P)}\right| dV_m}, \tag{10}$$

can be defined as a probability density, since it allows a measure of the probability to find p_m at $\mathbf{r}_m$ to be got in agreement with axioms (9a), (9b) and (9c).

Practically, $\eta_m^{(P)}$ differs from Ψ_m for an unknown constant factor and has also the advantage to give the sign of the pole. Thus, by

convention we assume $\eta_m^{(P)}$ as a probability measure for a P-source to occur at $\mathbf{r}_m$.

The $\eta_m^{(P)}$ function can readily be calculated knowing the mathematical expression of $\mathbf{s}(\mathbf{r}, \mathbf{r}_m)$, which is given the role of *source pole elementary scanner* (SPES).

In practice, as the source distribution responsible of the $\mathbf{A}(\mathbf{r})$ field is unknown, we virtually place a pole of unitary strength at the nodes of a grid filling a volume beneath the ground, wherein the targets are assumed to exist. Since the kernel $\mathbf{s}(\mathbf{r})$ is a known function, we can compute the SPOP value at each node, using a discretised form of the integral in Eq. (5). A positive SPOP value gives the probability with which a positive pole, placed where the SPOP value is computed, can be considered as responsible of the $\mathbf{A}(\mathbf{r})$ field, while a negative value gives the probability for a negative pole.

We show now a simplest example in order to let the main aspects of a SPOP tomography be soon clarified. The upper section in Fig. 2 shows two uniform spheres buried in a homogeneous half-space. The contrasts between the constitutive physical parameters of the two spheres and that of the host medium are of opposite sign. The anomaly field is supposed to be scalar, as e.g., the z-component of the gravity acceleration (Bouguer anomaly field), and the relative dataset to consist of measurements taken on the ground. The anomaly field map is shown in the middle horizontal slice in Fig. 2.

The 3D V-domain in this case collapses to a 2D S-domain, hence the volume integrals reduce to surface integrals extended over S, which can in general be a non-flat portion of the ground surface. The SPOP $\eta_m^{(P)}$ function is thus written as

$$\eta_m^{(P)} = C_m \int_S A(\mathbf{r}) s(\mathbf{r}, \mathbf{r}_m) dS, \tag{11}$$

where

$$C_m = \left[\int_S A^2(\mathbf{r}) dS \int_S s^2(\mathbf{r}, \mathbf{r}_m) dS \right]^{-1/2}. \tag{12}$$

Assuming the projection of S onto the (x, y)-plane can be fitted to a rectangle R of sides $2X$ and $2Y$ along the x-axis and y-axis, respectively, as in Fig. 1, using a topography function $g(z)$ given by

$$g(z) = \left[1 + (\partial z/\partial x)^2 + (\partial z/\partial y)^2 \right]^{1/2}, \tag{13}$$

Eq. (11) and Eq. (12) are regularized as follows

$$\eta_m^{(P)} = C_m \int_R A(\mathbf{r}) s(\mathbf{r}, \mathbf{r}_m) g(z) dxdy \tag{14}$$

and

$$C_m = \left[\int_R A^2(\mathbf{r}) g(z) dxdy \int_R s^2(\mathbf{r}, \mathbf{r}_m) g(z) dxdy \right]^{-1/2}, \tag{15}$$

where the integration intervals along the x-axis and y-axis are $[-X, X]$ and $[-Y, Y]$, respectively.

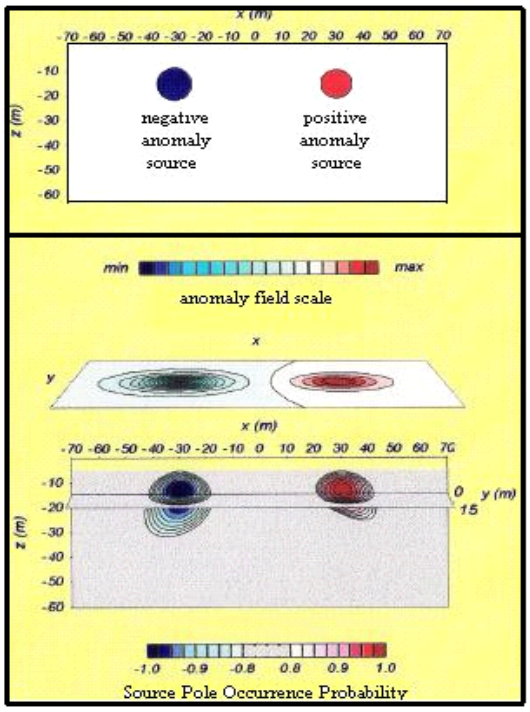

Figure 2. A qualitative example of the SPOP tomography. The two-sphere model generating anomalies of opposite sign (redrawn after [14]).

In the example of Fig. 2, S is taken a flat horizontal surface, hence from Eq. (13) it follows $g(z) = 1$.

The SPOP tomography is applied to image an occurrence probability space of P-sources, responsible of the anomalies detected on

the ground. To enhance the filtering property of the scanning process, it is advisable to use different integration surfaces in Eq. (14) and Eq. (15), by letting X and Y vary from sufficiently small values up to the size of the survey area. The smallest X and Y can be so chosen as to let the anomaly due to a P-source be fully contained in the R-domain centered over the pole. At each node, calculations must be done for all of the sizes of the R-domain. The highest value is assumed with its sign as the propermost SPOP value for that point.

The SPOP tomography for the two-sphere model is given in the lower section in Fig. 2. A smeared image is the peculiarity of this new type of target detection approach. Nevertheless, the position of the centers of the spheres is entirely retrieved, since they appear exactly where the SPOP highest absolute values have been found.

2.2. The Source Dipole Occurrence Probability

We now consider a generic n-th integral of the second double sum in Eq. (3), apply again Schwarz inequality and obtain for $\nu = x, y, z$

$$\left[\int_V \mathbf{A}(\mathbf{r}) \cdot \frac{\partial \mathbf{s}(\mathbf{r}, \mathbf{r}_n)}{\partial \nu_n} dV\right]^2 \leq \int_V A^2(\mathbf{r}) dV \int_V \left|\frac{\partial \mathbf{s}(\mathbf{r}, \mathbf{r}_n)}{\partial \nu_n}\right|^2 dV, \qquad (16)$$

from which a 3D *source dipole occurrence probability* (SDOP) function is defined as

$$\eta_{n\nu}^{(D)} = C_{n\nu} \int_V \mathbf{A}(\mathbf{r}) \cdot \frac{\partial \mathbf{s}(\mathbf{r}, \mathbf{r}_n)}{\partial \nu_n} dV, \qquad (17)$$

where

$$C_{n\nu} = \left[\int_V A^2(\mathbf{r}) dV \cdot \int_V \left|\frac{\partial \mathbf{s}(\mathbf{r}, \mathbf{r}_n)}{\partial \nu_n}\right|^2 dV\right]^{-1/2}. \qquad (18)$$

Again, for scalar anomaly field and kernel function, $\eta_{n\nu}^{(D)}$ becomes

$$\eta_{n\nu}^{(D)} = C_{n\nu} \int_V A(\mathbf{r}) \frac{\partial s(\mathbf{r}, \mathbf{r}_n)}{\partial \nu_n} dV, \qquad (19)$$

with $C_{n\nu}$ given by

$$C_{n\nu} = \left[\int_V A^2(\mathbf{r}) dV \cdot \int_V \left[\frac{\partial s(\mathbf{r}, \mathbf{r}_n)}{\partial \nu_n}\right]^2 dV\right]^{-1/2}. \qquad (20)$$

Therefore, at each $\mathbf{r}_n$ three values of $\eta_{n\nu}^{(D)}$ are calculated. They give a measure of the probability, obtained by the three components of a dipolar source (D-source) located at $\mathbf{r}_n$ as responsible of the $\mathbf{A}(\mathbf{r})$ set. Maxima of $|\eta_{n\nu}^{(D)}|$ are expected to focalize along boundaries.

The SDOP function can be calculated knowing the derivatives of the base function $\mathbf{s}(\mathbf{r}, \mathbf{r}_n)$. Each derivative is given the role of *source dipole elementary scanner* (SDES) function.

The SDOP 3D tomography of a geophysical dataset consists again in a scanning procedure operated now by the SDES function. We use a virtual D-source of unitary strength and place it at the same nodes of the grid, previously defined. We calculate the SDOP value at each node using a discretised form of the integral in Eq. (17). A non-null value of any of the three SDOP functions gives the probability which the relative moment component of a D-source, localized where the SDOP has been computed, obtain as responsible of the given $\mathbf{A}(\mathbf{r})$ field. The algebraic sign indicates now the direction of the dipole component along the axis to which the SDOP function under examination refers.

To show the peculiarity of the joint SPOP and SDOP imaging, Fig. 3(a) sketches two infinitely extended half-plates in contact, characterized by opposite contrasts of their constitutive parameter with respect to the host half-space. A scalar $A(\mathbf{r})$ function, simulating e.g., the Bouguer anomaly along a profile L, is drawn at top. The 3D V-domain thus reduces to a 1D L-domain, hence the volume integrals reduce to line integrals extended over L, which, in general, can be a non-straight line.

Assuming that the L-domain lies on a plane normal to the (x, y)-plane as the red line in Fig. 1, and its projection onto this plane is a segment of length $2X$ parallel to the x-axis, using a line regularization factor $h(x)$ expressed by

$$h(x) = \left[1 + (dz/dx)^2\right]^{1/2}, \tag{21}$$

the SPOP $\eta_m^{(P)}$ is expressed by

$$\eta_m^{(P)} = C_m \int_{-X}^{X} A(\mathbf{r}) s(\mathbf{r}, \mathbf{r}_m) h(x) dx, \tag{22}$$

where

$$C_m = \left[\int_{-X}^{X} A^2(\mathbf{r}) h(x) dx \int_{-X}^{X} s^2(\mathbf{r}, \mathbf{r}_m) h(x) dx \right]^{-1/2}. \tag{23}$$

Accordingly, since only the x-derivative can provide useful results, the $\eta_{nx}^{(D)}$ regularized integral can be written as

$$\eta_{nx}^{(D)} = C_{nx} \int_{-X}^{X} A(\mathbf{r}) \frac{\partial s(\mathbf{r}, \mathbf{r}_n)}{\partial x_n} h(x) dx, \tag{24}$$

where

$$C_{nx} = \left\{ \int_{-X}^{X} A^2(\mathbf{r}) h(x) dx \cdot \int_{-X}^{X} \left[\frac{\partial s(\mathbf{r}, \mathbf{r}_n)}{\partial x_n} \right]^2 h(x) dx \right\}^{-1/2}. \tag{25}$$

For the example in Fig. 3, L has been assumed a horizontal straight-line segment, hence, from Eq. (21), it follows $h(z) = 1$.

Figure 3(b) shows the result of the SPOP tomography along a vertical section through the profile, normal to the strike direction of the 2D target. Two pairs of SPOP nuclei of opposite sign appear at two different depth levels. The top pair is located inside the half-plates, while the bottom pair is placed below the half-plates with a larger separation than that of the top pair. In each pair the sign of each nucleus conforms to the sign of the constitutive parameter contrast of the relative plate. The highest SPOP absolute values belong to the deeper pair, thus providing an equivalent pair of P-sources compatible with the given anomaly profile. The top pair, which is characterized by smaller SPOP absolute values, appears, instead, to correctly outline the top level of the two half-plates.

The SDOP tomography is used to try to solve this uncertainty. The result of the SDOP tomography, using Eq. (24), is depicted in Fig. 3(c). A single D-source appears across the top portion of the boundary between the two half-plates. It extends down to the bottom wedge of the contact with still appreciable SDOP values. Its positive sign indicates that the horizontal component of the dipole moment lies along the x-axis positive direction rightwards, in full accord with the assumed model. This is an interesting result, which proves that the joint application of the SPOP and SDOP tomography is an efficient tool to discern among most probable equivalent solutions of a given inversion problem.

3. A FIELD APPLICATION: THE VESUVIUS CASE-HISTORY

Geophysics is largely applied to characterize physical and geometrical features of a volcanic apparatus and to study its feeding and plumbing

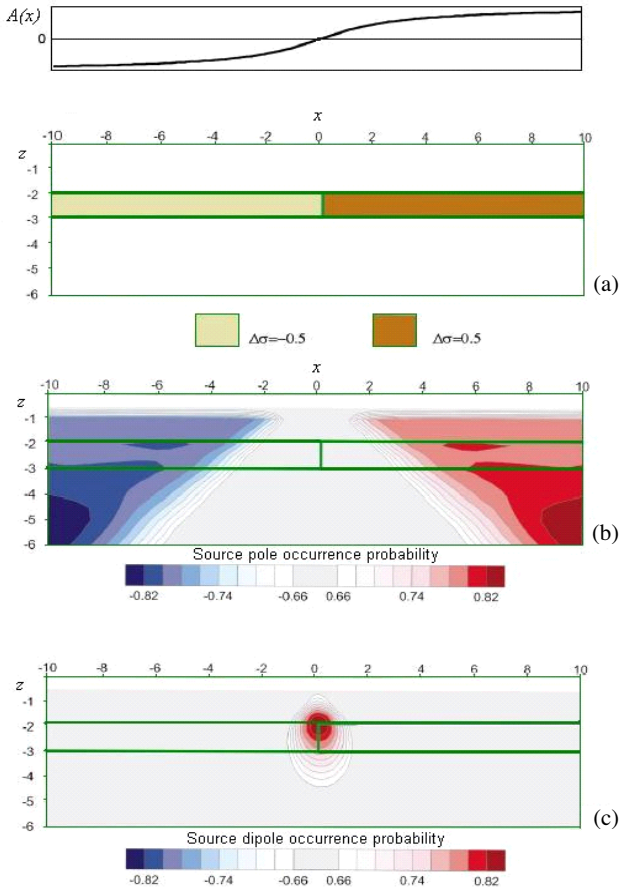

Figure 3. Application of SPOP and SDOP tomographies to a simulated prospection along a profile perpendicular to the strike of a 2D structure. (a) Cross-section of the 2D model and relative anomaly profile. (b) SPOP tomography. (c) SDOP tomography (redrawn after [9]).

systems. We show the results obtained from the application of the SPOP and SDOP tomography to the Vesuvius volcano (Naples, Italy).

Vesuvius is among the most surveyed volcanoes in the world for the great concern due to the high level of urbanization existing all around its slopes, closest to the city of Naples. A collection of recent studies about the volcanic structure and dynamics is given by [28].

Geophysical evidences so far collected indicate that Vesuvius grew

out of a depression of the carbonate basement with mean crustal density of about $2.5\,\mathrm{g/cm^3}$, overlain by less dense sediments. The shallow part of the volcano has been interpreted as a single central conduit surrounded by slowly cooled dikes. The summit cone appears to be made of altered volcanics. Going downwards, a high-to-low seismic P-wave velocity and resistivity boundary, estimated within a 8–10 Km depth range beneath the Vesuvius cone, has been assumed as the top of a magma chamber. These results were derived using standard modeling and inversion tools, except for the geoelectrical, self-potential and gravity data, which were analyzed by the original formulation of the SPOP tomography [9, 23–25].

We give now new results from the joint application of the SPOP and SDOP tomography to the geoelectric, self-potential and gravity datasets.

A satellite map of the volcanic area and the zones which have been investigated by the methods at issue are reported in Fig. 4.

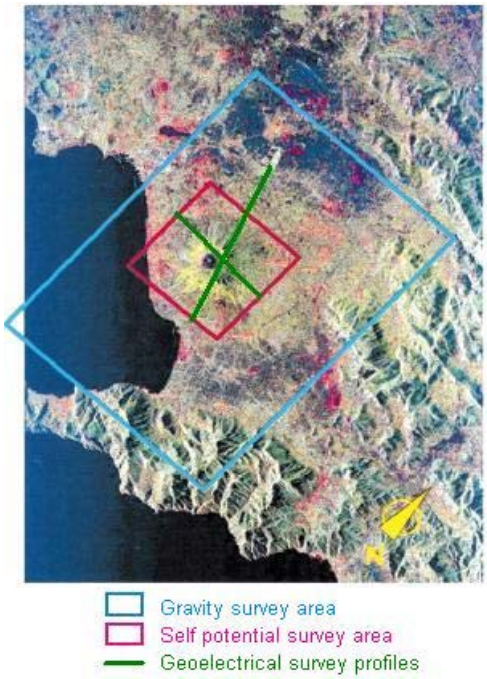

Figure 4. A satellite map of the Vesuvius volcanic area (Naples, Italy) with localization of the geoelectric profiles and self-potential and gravity survey areas (redrawn after [18]).

3.1. Geoelectrical Tomography

Figure 5 shows the geoelectric apparent resistivity pseudosections across the N-S (upper) and E-W (lower) profiles drawn in Fig. 4. The data were got using a bipole-bipole electrode array with a sampling step of 500 m. A square current waveform with a period of 30 s and maximum amplitude of 2 A was used to energize the ground. A stacking procedure was often adopted to extract the useful voltage signal from random noise. At the largest spacings and where the current electrodes contact resistance could not be sufficiently lowered, the stacking duration was extended up to one hour, at most. Each field datum was assigned at a pseudodepth equal to half the spacing between the centers of the active and passive bipoles, along the median axis across the line joining them. Corrections were occasionally made to account for height variations along the profile. Step-by-step displacement of the bipoles, together with step-by-step increase of the spacing between the two bipoles, provided a dense network of data points in the vertical pseudosection across each profile.

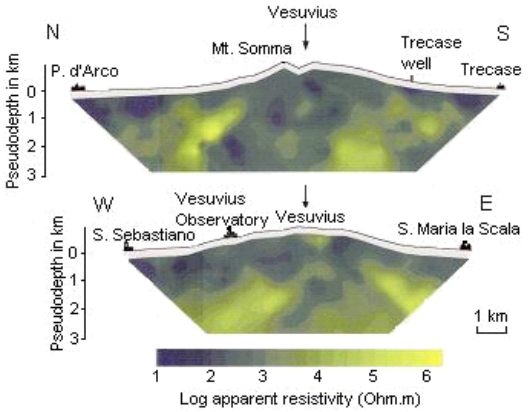

Figure 5. Geoelectrical apparent resistivity pseudosections relative to the N-S (top) and W-E (bottom) profiles shown in Fig. 4 (redrawn after [5]).

The SPOP tomographies across the N-S and E-W profiles have been elaborated using the approach by [12], which is reformulated as follows in the frame of this generalized theory.

The apparent resistivity dataset is a scalar function of x and z, where the x-axis is the horizontal straight-line at sea level lying in the vertical plane through the survey profile, and the vertical z-axis is taken positive downward. The origin is put at sea level midway along

the survey profile (see Fig. 6). The datum-domain is a surface S (the pseudosection), which can be divided in three sub-domains, S_1, S_2, S_3, as in Fig. 6, where top and bottom line topography functions are indicated by $z_{i,t}(x)$ and $z_{i,b}(x)$, $i = 1, 2, 3$, respectively. Referring to the definitions of the $\eta_m^{(P)}$ and $\eta_n^{(D)}$ functions, reported in Eq. (8) and Eq. (19), the anomaly function $A(\mathbf{r})$ is defined as

$$A(\mathbf{r}) = \Delta\rho_a(\mathbf{r}) \cong \sum_{m=1}^{M} \frac{\partial\rho_{a,0}\left(\mathbf{r}, \mathbf{r}_m\right)}{\partial\rho_{m,0}} \Delta\rho_m, \tag{26}$$

where $\Delta\rho_a(x, z)$ is the departure of the detected apparent resistivity $\rho_a(x, z)$ from a reference apparent resistivity $\rho_{a,0}(x, z)$, and $\Delta\rho_m$ is the difference between the true resistivity ρ_m of the m-th source cell (pole) and the resistivity $\rho_{m,0}$ in the same cell imposed by the reference model. In Eq. (25), the scanner function $s(x, z)$ is the Frechet derivative of the reference apparent resistivity function for a resistivity perturbation in the m-th cell [12, 15, 19].

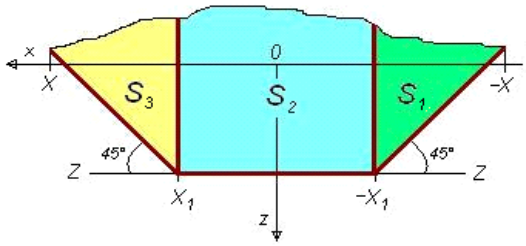

Figure 6. The S-domain partition for the computation of the SPOP and SDOP tomography of the pseudosections reported in Fig. 5.

Referring to the geometry in Fig. 6, the SPOP function becomes

$$\eta_m^{(P)} = C_m \int\limits_{S_1+S_2+S_3} f_1 f_2 dx dz, \tag{27}$$

where

$$C_m = \left(\int\limits_{S_1+S_2+S_3} f_1^2 dx dz \cdot \int\limits_{S_1+S_2+S_3} f_2^2 dx dz \right)^{-1/2}, \tag{28}$$

$f_1 = \Delta\rho_a(\mathbf{r})$ and $f_2 = \partial\rho_{a,0}(\mathbf{r}, \mathbf{r}_m)/\partial\rho_{m,0}$. The integration intervals along the x-axis and z-axis are, respectively:

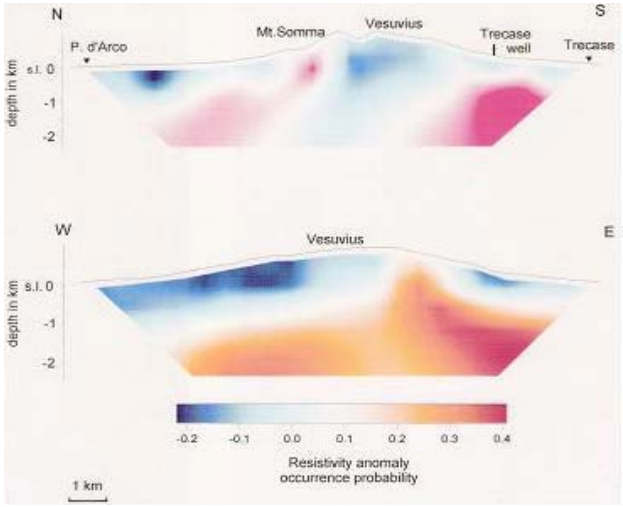

Figure 7. Geoelectrical sections of the SPOP tomography at Vesuvius across the N-S (top) and E-W (bottom) profiles shown in Fig. 4 (redrawn after [25]).

$[-X, -X_1]$ and $[z_{1,t}(x), z_{1,b}(x) = (Z + X_1) + x]$ in S_1,
$[-X_1, X_1]$ and $[z_{2,t}(x), Z]$ in S_2,
$[X_1, X]$, and $[z_{3,t}(x), z_{3,b}(x) = (Z + X_1) - x]$ in S_3.

Figure 7 shows the resulting SPOP tomographies across the N-S (top) and E-W (bottom) profiles.

The N-S SPOP tomography shows a well resolved P-source pattern [25]. The northern shallow negative SPOP nucleus identifies the core of a conductive structure likely ascribable to marine water-bearing sediments filling the Pomigliano d'Arco plain. The shallow central positive nucleus, beneath the Mt. Somma caldera northern rim, highlights the core of a resistive structure likely associable to a zone of poorly fractured and dry volcanics, as e.g., a slowly cooled dike. The following shallow negative nucleus, beneath the summit part of the Vesuvius edifice, identifies the core of a conductive structure, which leads to admit that the Vesuvius chimney is likely occluded by water-rich and mineral-rich fine deposits. Finally, the southern deeper positive nucleus identifies a resistive block likely associable to the thick sequence of submarine lavas and underlying carbonatic basement, in accord with the stratigraphic column deducted from the Trecase well, drilled by the Italian Oil Agency AGIP [27, 28].

In the E-W SPOP tomography, the westward shallow negative

nucleus identifies the core of a conductive structure very likely ascribable to a thick aquifer trapped along the western slopes of the volcano. The weak positive nucleus that appears right beneath the Somma caldera eastern rim identifies the core of a resistive body ascribable to the previously mentioned dike structure. No evidence of the central obstructed chimney is, however, deducted, likely because the E-W profile, placed north of the top cone of Vesuvius, does not cross the bowl-shaped summit part of the volcano central conduit. Another shallow negative zone appears on the eastern portion of the section. It identifies the core of a conductive layer very likely ascribable to the aquifer trapped along the eastern slopes of Vesuvius. Finally, the eastern and central-western deeper positive nuclei highlight resistive blocks likely referable to east to the faulted carbonatic slab cropping out a few Km inland, and in the central part to a pile of compact lava flows overlying the said slab, gently deepening towards the Tyrrhenian sea.

We show now the results of the SDOP tomography. The expressions of $\eta_{n\nu}^{(D)}$ and $C_{n\nu}$ are written following the procedure used to derive Eq. (27) and Eq. (28). They are

$$\eta_{n\nu}^{(D)} = C_{n\nu} \int\limits_{S_1+S_2+S_3} f_1 f_3 dxdz, \tag{29}$$

$$C_{n\nu} = \left(\int\limits_{S_1+S_2+S_3} f_1^2 dxdz \cdot \int\limits_{S_1+S_2+S_3} f_3^2 dxdz \right)^{-1/2}, \tag{30}$$

where $f_3 = \partial[\partial\rho_{a,0}(\mathbf{r}, \mathbf{r}_n)/\partial\rho_{n,0}]/\partial\nu_n$.

Figures 8 and 9 show the $\eta_{nx}^{(D)}$ and $\eta_{nz}^{(D)}$ tomographies, respectively, as, obviously, only the x and z derivatives can be elaborated with data collected along profiles.

The SDOP tomographies across the N-S profile (top sections in Fig. 8 and Fig. 9) show a D-source pattern quite compatible with the previous P-source pattern. A notable positive D-source appears in Fig. 8 beneath the Mt. Somma northern rim, exactly amid the shallow P-source pair with opposite sign, previously observed in the top section of Fig. 7. This D-source, combined with the negative D-source emerging right at the same place in the SDOP tomography of Fig. 9, likely marks the existence of a sharp boundary separating the two different blocks previously associated with the adjacent P-sources. The opposite sign of these SDOP nuclei and their apparent prolate shape allow the trace of the hypothesized sharp boundary to be imaged nearly as a leftward downverging segment. A second

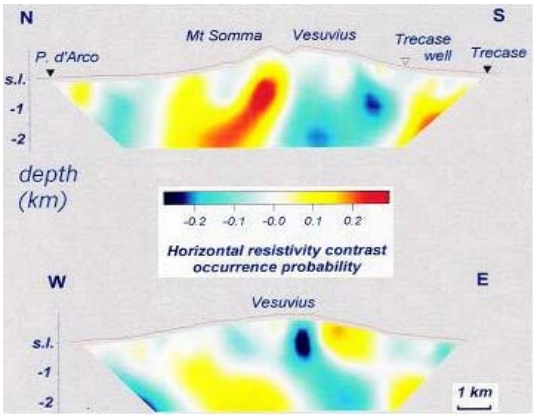

Figure 8. Geoelectrical sections of the x-component SDOP tomography at Vesuvius across the N-S (up) and E-W (down) profiles shown in Fig. 4.

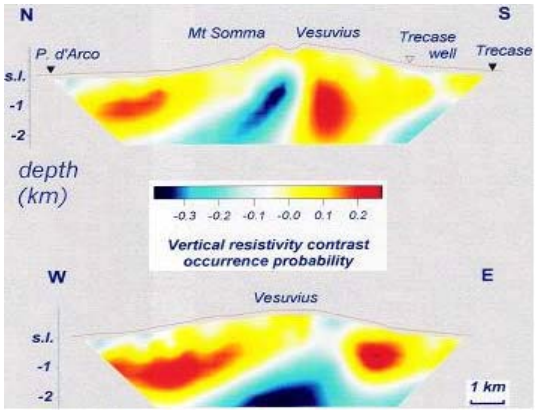

Figure 9. Geoelectrical sections of the z-component SDOP tomography at Vesuvius across the N-S (up) and E-W (down) profiles shown in Fig. 4.

remarkable feature of the top tomography in Fig. 8 is the pair of negative D-sources located between the Vesuvius summit cone and the Trecase well. This pair, together with the nucleus appearing in the top tomography of Fig. 9, in the same sector of the section, likely demarcate a stepped boundary separating the volcano edifice from the underlying sequence of submarine lavas and carbonates. The sign of the x- and z-component of these D-sources is congruent with the sign of the P-

sources located in that portion of the section. The last notable feature of the N-S profile is the positive nucleus perched in the northernmost sector of the $\eta_{nz}^{(D)}$ tomography of Fig. 9, in the Pomigliano d'Arco area. It can likely be ascribed to a horizontal boundary dividing the shallow water-bearing sediments from the underlying piles of compact volcanics.

The E-W $\eta_{nx}^{(D)}$ tomography in Fig. 9 shows only a negative, vertically prolate nucleus beneath Vesuvius. It very likely highlights a sharp lateral passage from the conductive top central part of Vesuvius to the resistive, nearly vertical wall beneath the eastern rim of the Mt. Somma caldera, interpreted as compact dyke. The E-W $\eta_{nz}^{(D)}$ tomography provides some further information. In fact, the western widely prolate positive nucleus may likely be associated to a nearly horizontal boundary between the shallow water-bearing layer and the underlying pile of compact lava flows. Similarly, the eastern positive nucleus can likely be interpreted as the trace of a nearly horizontal sharp transition from the upper water-bearing volcanic sequence to the underlying carbonate basement. Finally, the deep negative nucleus can be related to a horizontal transition from a pile of compact lavas to a fractured altered block of the carbonatic slab.

3.2. Self-potential Tomography

A dataset consisting of 1250 self-potential (SP) measures was collected using the gradient technique by displacing a 100 m long passive bipole continuously along a mesh of interconnected profiles over an area of $12 \times 12\,\mathrm{Km}^2$ (Fig. 4) [5]. Due to the difficulty of access and the vastness of the area, the SP profiles were randomly distributed. SP drifts, caused by external factors as temperature excursion, rainfall and infiltration, were corrected by measuring each profile forth and back and then distributing the SP closure error homogenously along the profile [4, 5]. Furthermore, the cumulative error due to electrode polarization was avoided, by alternating the role of the two electrodes of the bipole at each subsequent measurement along the profile [4, 5]. The top slice in Fig. 10 shows the original SP map in mV.

In the case of SP fields, the $\mathbf{A}(\mathbf{r})$ vector function is represented by the steady natural electrical field vector on the ground and the SPES vector function $\mathbf{s}(\mathbf{r}, \mathbf{r}_m)$ is explicated as

$$\mathbf{s}(\mathbf{r}, \mathbf{r}_m) = \frac{\mathbf{r} - \mathbf{r}_m}{|\mathbf{r} - \mathbf{r}_m|^3}. \tag{31}$$

The SPOP function $\eta_m^{(P)}$ has been computed using Eq. (5) and

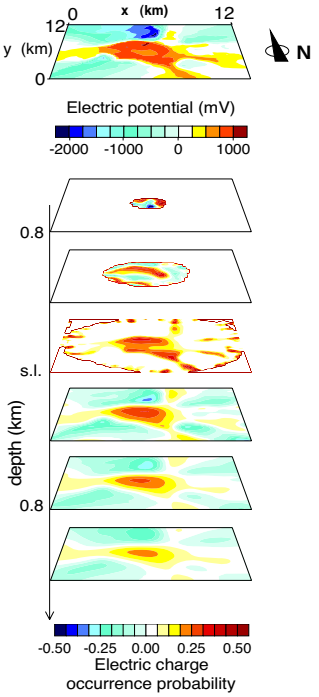

Figure 10. The SP SPOP tomography of Vesuvius. The top slice is the reference SP anomaly map.

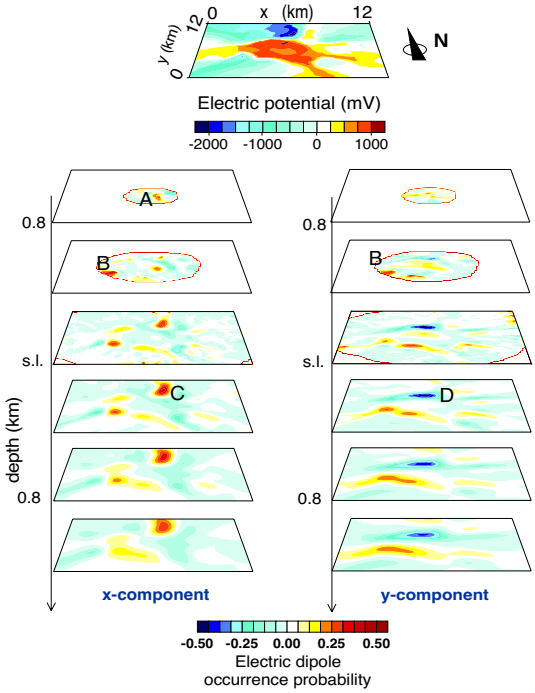

Figure 11. The SP SDOP tomography of Vesuvius. The top slice is the reference SP anomaly map.

Eq. (6), and the SDOP function $\eta_{nv}^{(D)}$ using Eq. (17) and Eq. (18), by applying the topography regularization function given by Eq. (13).

In Fig. 10, the topmost slice of the $\eta_m^{(P)}$ sequence shows a negative P-source in correspondence with the summit Vesuvius cone. It is circled by positive cores extending down to 0.4 Km a.s.l., which appear to delineate the Mt. Somma caldera rim, mostly its northeastern and southwestern arcs. At sea level, a positive core appears again in correspondence with the cone, together with sequences of aligned positive nuclei indicating the main radial fracture system crossing the volcanic area. Finally, at sea level a roughly ring distribution of positive nuclei appears to highlight the outer border of the whole volcanic area. This positive ring pattern is accompanied by weak negative cores, occupying intermediate positions and reaching the

highest absolute values in the slice at 0.4 Km of depth b.s.l., above all that appearing in the northwestern sector.

As is well documented, in hydrothermal systems SP signals are caused mainly by electrokinetic effects. Generally, in volcanic areas, positive anomalies correspond to upward migrating fluids, while negative ones to downward fluid movement [31]. Accepting such a model, the top central negative nucleus would outline the position of the main path for meteoric waters infiltration, in correspondence with the Vesuvius crater. The inner crown of positive cores would instead indicate the sites of thermal fluids uprising. This plus/minus feature may thus represent the signature of a fluid convection mechanism within a thermal field localized above sea level inside the mountain.

The outer crown of positive cores together with the positive radial trends at sea level, may, as previously, be assigned to dominant paths for uprising thermal fluids. Accordingly, the negative nuclei wedged at 400 m of depth b.s.l. inside the positive radial strips are likely to indicate the cores of deep feeding zones within a larger thermal convection system extended below the whole volcanic area.

The SDOP tomography has been applied to the SP map in order to get a better resolution of the boundary zones. Fig. 11 illustrates the $\eta_{nx}^{(D)}$ and $\eta_{ny}^{(D)}$ tomographies, as only the two derivatives with respect to x and y can bring to useful results. The most evident nuclei are highlighted by a capital letter, which, when it appears in both the right-hand and left-hand sequence, it means that the corresponding nuclei belong to the same D-source.

The D-source "A", appearing on the slice of $\eta_{nx}^{(D)}$ at 0.8 Km a.s.l., and the source pair "B", appearing on the slices of $\eta_{nx}^{(D)}$ and $\eta_{ny}^{(D)}$ at 0.4 Km a.s.l., would likely indicate the core of an ideal lateral boundary, within the upper thermal system, dividing the charging area inside the Vesuvius conduit from the discharge areas along the northeastern and southwestern arcs of the Somma caldera rim. The D-sources "C" and "D" in the $\eta_{nx}^{(D)}$ and $\eta_{ny}^{(D)}$ tomography, respectively, reaching SDOP maximum absolute values at about 0.4 Km b.s.l., well outline the boundaries of the wedged feature evidenced in the SPOP tomography.

3.3. Gravity Tomography

The Bouguer residual map in the Vesuvius area, drawn in the top slice of Fig. 12, was elaborated by [3] by means of 1850 data distributed with an average density of 1 station per Km^2 within an area of $26.6 \times 37\,\mathrm{Km}^2$. A density of $2.3\,\mathrm{g/cm}^3$ was used for the slab and terrain corrections and a S35°W trend of 0.9 mgal/Km was subtracted from the original values. The main large-scale features are a wide gravity low, extending

Figure 12. The gravity SPOP tomography of Vesuvius. The top slice is the reference gravity survey map.

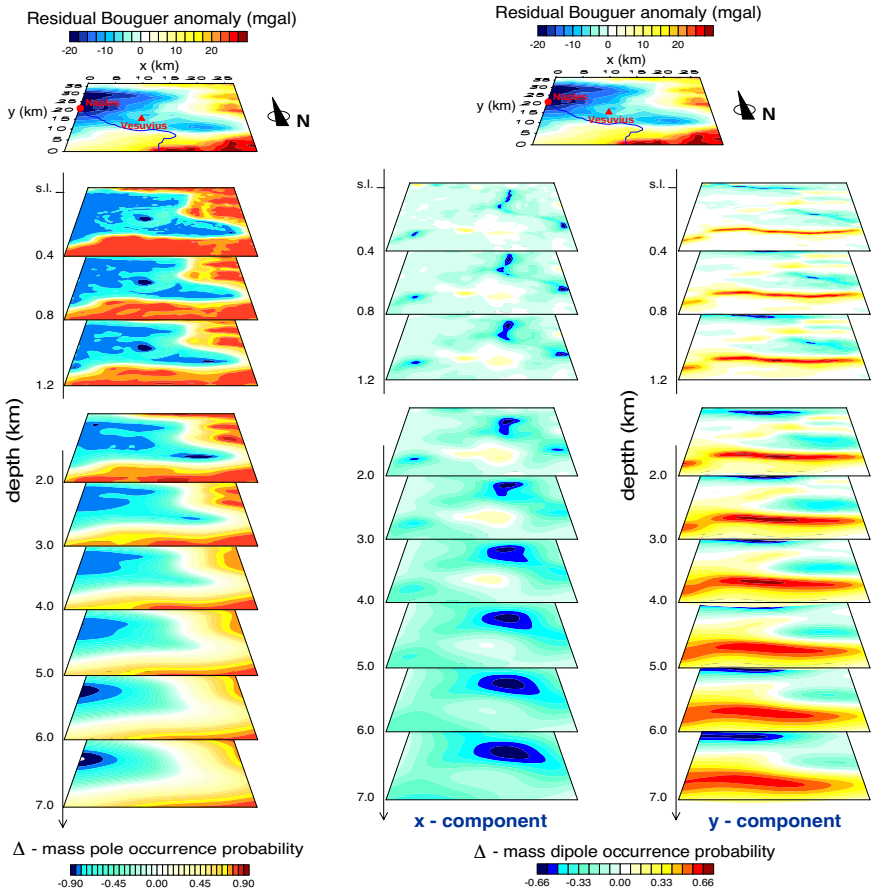

Figure 13. The gravity SDOP tomography of Vesuvius. The top slice is the reference gravity anomaly map.

from the northwestern side to the whole central area, and a gravity high bordering the negative anomaly along the northeastern and southern sectors of the map. The gravity low represents quite well the huge structural depression within which the whole volcanic activity grew, while the gravity high closely depicts the structural highs consisting of the carbonate massifs, bordering the Campanian plain and reaching southwestwards the whole Sorrento peninsula [27].

The sequence of slices in Fig. 9 displays the 3D tomography of

the SPOP function, where the P-sources are assimilated to the mass centers of bodies with either a surplus or a deficit of mass (Δ-mass) with respect to the hosting medium. $A(\mathbf{r})$ is now the scalar Bouguer anomaly dataset (i.e., the z-component of the gravity field) and the scalar SPES function is explicated as

$$s(\mathbf{r}, \mathbf{r}_m) = \frac{z_m - z}{|\mathbf{r}_m - \mathbf{r}|^3}. \tag{32}$$

The SPOP function has been calculated using Eq. (8) and Eq. (6), and the SDOP function using Eq. (19) and Eq. (20), by applying as before the regularization function given by Eq. (13).

A negative Δ-mass accumulation characterizes the northwestern and mid-eastern part of the survey area. Three distinct negative nuclei aligned SE-NW emerge at different depth levels inside this huge volume. The easternmost nucleus expands inside the range 1.2–2 Km b.s.l., whereas the signature of the northwestern nucleus starts at about 6 Km of depth b.s.l. and deepens to about 7 Km b.s.l.. The third core outcrops in the central sector below Vesuvius from about 0.4 Km a.s.l. to about 1.6 Km b.s.l.. The whole huge depression with the three lighter blocks is surrounded to east and south by a belt of rocks denser than 2.3 g/cm^3 but with less defined nuclei. Two denser blocks appear at the eastern and southern margins of the tomospace. Both nuclei have a very limited extent from 1.6 Km b.s.l. down to 2 Km b.s.l.

In order to obtain more information, we show now the results of the SDOP tomography to detect the presence of Δ-mass dipoles ascribable to discontinuities. Fig. 13 shows the $\eta_{nx}^{(D)}$ and $\eta_{ny}^{(D)}$ tomographies, as only the two derivatives with respect to x and y can bring to meaningful results.

The SDOP tomography provides a detailed image of the boundaries of the huge volume with less dense materials appearing in the northwestern and central-eastern parts of the surveyed area. The northern, eastern and southern lateral boundaries of this volume are well outlined down to at least 3–4 Km b.s.l. The sign of the SDOP nuclei reflects the sign of the dipole moment components, in conformity with the coordinate reference plane (x-axis and y-axis positive eastwards and northwards, respectively).

4. CONCLUSION

The interpretation of electrical and, more generally, electromagnetic survey data is likely the most complex topic in geophysics, independently of the investigation depth range and area of

intervention. Given the importance of the related applications, this argument always attracts many specialists worldwide, as documented by the vast literature especially of the last decade, in conjunction with the computer technology increasing efficacy (see, e.g., [1, 2, 6, 8, 10, 22, 26, 29, 30], to quote a few most recent papers freely available online).

In this paper, adhering to the propensity interpretative approach of modern science [11], a probability tomography method has been developed in order to analyze geoelectrical and other geophysical vector or scalar field datasets. The purpose of the new method is to get rid of some restrictive approaches that are conventionally adopted to interpret geophysical datasets, usually derived from very simplistic assumptions about the physical reality, often dictated by some more or less idealized or exotic geological assumptions. We postulate that the geophysical reality consists of two kinds of reality, say actual and potential, where we mean for actual what we get when we can directly explore the geophysical entity, and for potential the largest spread of structural compositions compatible with the measured datasets.

We have revisited the source pole tomography, already documented in some previous papers, in order to introduce in a direct and more compact way the innovative argument of the source dipole tomography.

The new method has been tested on a few synthetic examples, which demonstrate that the spectrum of potential solutions of a geophysical interpretative problem can coexist, from a probabilistic point of view, with the actual model, i.e., with the model which can then be proved to closely represent the real situation.

An application to the Vesuvius volcano (Naples, Italy), to image polar and dipolar sources of geoelectrical, self-potential and gravity anomaly datasets collected over the whole volcanic area, has been shown.

The most important results that have been achieved can be synthesized as follows:

1. a slowly cooled compact magmatic dike is likely to exist beneath the Mt. Somma caldera northern rim;
2. the Vesuvius conduit is likely to be occluded by water- and mineral-rich fine deposits;
3. a thick water-bearing horizon is likely to be trapped along the western and eastern slopes of the volcano;
4. a fluid convection mechanism is likely to be active in a geothermal reservoir perched above sea level inside the Vesuvius complex;

5. a larger thermal convection system extended below the volcanic area is likely to exist in the first 0.5 Km b.s.l.;
6. the whole Mt. Somma-Vesuvius apparatus is likely to be emplaced in a very large and thick tectonic depression.

We remark that, generally, the zones where $\eta_m^{(P)}$ and $\eta_n^{(D)}$ functions reach the highest absolute values, are, from a probabilistic point of view, the candidate places where to hypothesize the presence of the core-and-boundary sources of the anomalies observed in the datum space. In the Somma-Vesuvius area, the SPOP and SDOP nuclei with the highest absolute values appear, in fact, as the most suitable places where to ascribe the features listed above. We do not exclude, however, that other points in the tomospace, even if characterized by lower absolute values of the $\eta_m^{(P)}$ and $\eta_n^{(D)}$ functions, if properly combined can represent a potential source model compatible with the observed anomaly field and acceptable from the volcanological point of view. As is well known, in active volcanic areas an extensive validation of the geophysical structural modelling is practically impossible, because of the absence of an overall exploitation interest. The best way to approach a likely model of the area is to integrate different geophysical methods and be aware of the outcomes from other related disciplines, like geochemistry, observational volcanology and petrology, as we have tried to do in this paper.

ACKNOWLEDGMENT

Study carried out with financial support from the Italian Ministry of Education, University and Research (PRIN 2000 project), the European Commission (TOMAVE project) and the Italian Group of Volcanology of the National Research Council.

REFERENCES

1. Abo-Seida, O. M., "Far-field due to a vertical magnetic dipole in sea," *Journal of Electromagnetic Waves and Applications*, Vol. 20, No. 6, 707–715, 2006.
2. Capineri, L., D. Daniels, P. Falorni, O. Lopera, and C. Windsor, "Estimation of relative permittivity of shallow soils by using the Ground Penetrating Radar response from different buried targets," *Progress In Electromagnetics Research Letters*, Vol. 2, 63–71, 2008.

3. Cassano, E. and P. La Torre, "Geophysics," *Somma-vesuvius*, R. Santacroce (ed.), Vol. 114/8, 175–196, Quaderni de La Ricerca Scientifica, CNR, Rome, 1987.
4. Di Maio, R., V. Di Sevo, S. Giammetti, D. Patella, S. Piscitelli, and C. Silenziario, "Self-potential anomalies in some Italian volcanic areas," *Annals of Geophysics*, Vol. 39, 179–188, 1966.
5. Di Maio, R., P. Mauriello, D. Patella, Z. Petrillo, S. Piscitelli, and A. Siniscalchi, "Electric and electromagnetic outline of the Mount Somma-Vesuvius structural setting," *Journal of Volcanology and Geothermal Research*, Vol. 82, 219–238, 1998.
6. Franceschini, G., A. Abubakar, T.M. Habashy, and A. Massa, "A comparative assessment among iterative linear solvers dealing with electromagnetic integral equations in 3D inhomogeneous anisotropic media," *Journal of Electromagnetic Waves and Applications*, Vol. 21, No. 7, 899–914, 2007.
7. Gnedenko, B. V., *Kurs Teorii Verojatnostej*, Mir, Moscow, Published in Italian as *Teoria Della Probabilità*, Editori Riuniti, Rome, 1979.
8. Habashy, T. M. and A. Abubakar, "A generalized material averaging formulation for modelling of the electromagnetic fields," *Journal of Electromagnetic Waves and Applications*, Vol. 21, No. 9, 1145–1159, 2007.
9. Iuliano, T., P. Mauriello, and D. Patella, "Looking inside Mount Vesuvius by potential fields integrated geophysical tomographies," *Journal of Volcanology and Geothermal Research*, Vol. 113, 363–378, 2002.
10. Liu, L., K. Li, and W.-Y. Pan, "Electromagnetic field from a vertical electric dipole in a four-layered region," *Progress In Electromagnetics Research B*, Vol. 8, 213–241, 2008.
11. Marshall, I. and D. Zohar, *Who's Afraid of Schrödinger's Cat?* Bloomsbury, London, 1997.
12. Mauriello, P. and D. Patella, "Resistivity anomaly imaging by probability tomography," *Geophysical Prospecting*, Vol. 47, 411–429, 1999.
13. Mauriello, P. and D. Patella, "Gravity probability tomography: A new tool for buried mass distribution imaging," *Geophysical Prospecting*, Vol. 49, 1–12, 2001.
14. Mauriello, P. and D. Patella, "Localization of maximum-depth gravity anomaly sources by a distribution of equivalent point masses," *Geophysics*, Vol. 66, 1431–1437, 2001.
15. Mauriello, P. and D. Patella, "Introduction to tensorial resistivity

probability tomography," arXiv:physics/0512147v1, 1–8, 2005.

16. Mauriello, P. and D. Patella, "Localization of magnetic sources underground by a data adaptive tomographic scanner," arXiv:physics/0511192v2, 1–15, 2005.
17. Mauriello, P. and D. Patella, "Imaging polar and dipolar sources of geophysical anomalies by probability tomography. Part I: Theory and synthetic examples," arXiv:physics/0602056v1, 1–6, 2006.
18. Mauriello, P. and D. Patella, "Imaging polar and dipolar sources of geophysical anomalies by probability tomography. Part II: Application to Vesuvius volcanic area," arXiv:physics/0602057v1, 1–7, 2006.
19. Mauriello, P. and D. Patella, "Resistivity tensor probability tomography," *Progress In Electromagnetics Research B*, Vol. 8, 129–146, 2008.
20. Mauriello, P. and D. Patella, "Localization of magnetic sources underground by a probability tomography approach," *Progress In Electromagnetics Research M*, Vol. 3, 27–56, 2008.
21. Mauriello, P., D. Monna, and D. Patella, "3D geoelectric tomography and archaeological applications," *Geophysical Prospecting*, Vol. 46, 43–570, 1998.
22. Ozdemir, C., S. Demirci, and E. Yigit, "Practical algorithms to focus B-scan GPR images: theory and application to real data," *Progress In Electromagnetics Research B*, Vol. 6, 109–122, 2008.
23. Patella, D., "Introduction to ground surface self-potential tomography," *Geophysical Prospecting*, Vol. 45, 653–681, 1997.
24. Patella, D., "Self-potential global tomography including topographic effects," *Geophysical Prospecting*, Vol. 45, 843–863, 1997.
25. Patella, D. and P. Mauriello, "The geophysical contribution to the safeguard of historical sites in active volcanic areas. The Vesuvius case-history," *Journal of Applied Geophysics*, Vol. 41, 241–258, 1999.
26. Popov, A. V. and V. V. Kopeikin, "Electromagnetic pulse propagation over non-uniform earth surface: Numerical simulation," *Progress In Electromagnetics Research B*, Vol. 6, 37–64, 2008.
27. Principe, C., M. Rosi, R. Santacroce, and A. Sbrana, "Explanatory notes to the geological map," *Somma-vesuvius*, R. Santacroce (ed.), Vol. 114/8, 11–51, Quaderni de La Ricerca Scientifica, CNR, Rome, 1997.
28. Spera, F. J., B. De Vivo, R. A. Ayuso, and H. E. Belkin, "Special issue: Vesuvius," *Journal of Volcanology and Geothermal Research*, Vol. 82, 1–247, 1998.

29. Van den Bosch, I., S. Lambot, M. Acheroy, I. Huynen, and P. Druyts, "Accurate and efficient modeling of monostatic GPR signal of dielectric targets buried in stratified media," *Journal of Electromagnetic Waves and Applications*, Vol. 20, No. 3, 283–290, 2006.
30. Wang, Y.-L., W. Ren, and K. Li, "Exact transient field of a horizontal electric dipole excited by a Gaussian pulse on the surface of one-dimensionally anisotropic medium," *Progress In Electromagnetics Research B*, Vol. 8, 307–318, 2008.
31. Zlotnicki, J. and Y. Nishida, "Review on morphological insights of self-potential anomalies on volcanoes," *Survey in Geophysics*, Vol. 24, 291–338, 2003.